DOI: 10.13009/EUCASS2023-751
Aerospace Europe Conference 2023 – 10TH EUCASS – 9TH CEAS

Thermal image generation tool for spacecraft relative navigation in proximity maneouvering phases

Matteo Quirino⋆† *and Michelle Lavagna*⋆
⋆*Department of Aerospace Science and Technology, Politecnico di Milano*
Via La Masa 34, Milano, Italy 20156
matteo.quirino@polimi.it · michelle.lavagna@polimi.it
†Corresponding author

Abstract

On-orbit autonomous relative navigation performance strongly depends on both sensor suite and state reconstruction selection. Whenever that suite relies on image-based sensors working on visible spectral band, the illumination conditions strongly affect the accuracy and robustness of the state reconstruction outputs. To cope with that limitation the ASTRA PoliMi team started investigating the effectiveness of exploiting image sensors active in the IR spectral band, not limited by the lighting conditions. To run effective and comprehensive testing and validation campaigns on navigation algorithms a large dataset of images is requested, either available or easy to settle in the visible band, not trivial and not accessible for the thermal band. The paper presents the full open-source tool under development at PoliMi-ASTRA that exploits an accurate finite volume thermal model of a celestial object and creates thermal images based on the camera dynamic. In particular, a use case of flight proximity with small celestial bodies is discussed. The thermal model relies on open CFD code (OpenFOAM) pushed to catch the finest details of the terrain the temperature field is processed in order to compute the view factors between the camera and each face of the mesh, thus the radiative flux emitted by each face is extracted. Such data feeds the rendering engine (Blender) that together with the camera position and attitude outputs the thermal image. The complete pipeline, fed by orbiting target and the imaging sensor kinematic, outputs a proper synthetic thermal image dataset, exploitable either by a relative navigation block or any other scope of research. Furthermore, in the same framework, the dataset could be used as input for a thermal sensor model providing full customization of the output. The tool performance is critically discussed and applied for two typical proximity scenarios, asteroid and artificial satellite, for both cases challenges and capabilities of the implemented tool for synthetic thermal images are highlighted.

1. Introduction

Thermal images have an incredible advantage over optical images since no light sources are needed. This has a tremendous impact on the navigation reliability of a space mission, enabling the spacecraft to see the dark regions of planets and asteroids or detect other spacecraft in the dark.

As an example, operating around an asteroid during proximity phases requires continuous pointing and navigation even during night phases and thermal cameras can guarantee the detectability of the asteroid's shape in all conditions. Furthermore, the biggest advantage of thermal images over optical ones is that they enable the detection of objects in the deep sky more easily despite the lower instrument resolution.[6,7,11] Indeed, optical cameras have more pixels which translate into bigger spatial resolution and lower detection limits for the size of the objects, but optical images capture all the star lights with a resulting image full of bright spots other than the target. By looking at real thermal images for the detection of asteroids and planets, the target is the only bright spot in the image, making the detection much easier for navigation purposes.[12]

These were just the two biggest advantages of thermal images, many other applications are made possible thanks to TIR images such as site selection in dark regions, deployable satellite tracking and navigation and target marking.[11] Despite the unquestionable advantages of TIR images, the literature on how to create synthetic thermal images is still very scarse (for an accurate literature review the reader can refer to[6,7]) but at the same time, the possibility to create thermal images is fundamental for any mission involving thermal cameras for the following reasons:

1. Thermal image data sets can be created to train and test navigation algorithms in all mission phases.

DOI: 10.13009/EUCASS2023-751

2. Test software and hardware in the loop electronics, such as image processing boards.

3. Simulate the scientific output of the mission.

Given the importance of the above points, the paper describes a method to create thermal images starting from high geometrical accuracy thermal simulation results and reports the application of the method for spacecraft and asteroids case. Most of the thermal models proposed in the literature for such applications consist in 1D thermal models that despite their simplicity are not able to simulate the different thermal inertia properties or thermal contact connections between different parts of the object.[9,14,15] For the asteroid case, boulders of different sizes are present on the surface, and each of them requires proper thermal contact settings. This is even more important for the spacecraft scenario. The proposed method differs from the current methods in literature as it uses a 3D finite volume method to compute the temperature field of the object accounting for all the different regions thermal properties. The generation of thermal image is then performed using a rendering engine software and finally, two thermal camera models are proposed as future starting points to simulate the actual output of the instrument.

2. Thermal modelling

The section reports the major steps for the creation of the thermal image starting from the finite volume thermal model up to the thermal camera model output.

2.1 Finite volume thermal model:

The temperature field of the object is computed using the finite volume open source code OpenFOAM. The code offers the geometrical accuracy required to create realistic thermal images and the flexibility needed to interface with the rendering engine. For the description of the code and the numerical testing the reader can refer to,[16,17] the code has been compared to real thermal vacuum test data in a CubeSat scenario proving to be reliable in computing the temperature field, moreover, preliminary mono-material cases using such code are presented in.[3,6–8]

For the multi-region case presented in the article, different properties are assigned to the different parts of the object, from the resulting temperature field, each mesh face temperature is available together with the face orientation which is fundamental for the view factor computation as reported in the next sections.

2.2 Radiation modelling

There are two types of thermal cameras: photon counters and microbolometers.[1] The article focuses on the latter one being more versatile and more robust with respect to the former ones, furthermore, they have a wide space heritage. For more details, the reader can refer to.[2,5,13] Microbolometer pixels are sensitive to the heat flux that hits the pixel thus the goal is to compute the heat flux per unit area emitted by each mesh face in the frequency spectrum of the thermal camera, for microbolometers, it is the LWIR spectrum from 8 μm to 14 μm, therefore the heat flux emitted in this range by each face is given by:[13]

$$q_{out}(T) = \pi \int_0^\infty \varepsilon(\lambda)\, B(\lambda, T)\, R(\lambda)\, d\lambda \tag{1}$$

Where $\varepsilon(\lambda)$ is the emissivity, $B(\lambda, T)$ is the Max-Plank equation, $R(\lambda)$ is a function that goes from 0 to 1 in the LWIR range and accounts for the camera optics attenuation and instrument sensitivity in the LWIR range.[13] In the presence of the atmosphere is the parameter that accounts for the atmospheric attenuation in the LWIR range due to H_2O and CO_2, for space application is a continuous curve.

The next step is to compute the heat flux emitted by an infinitesimal part of a generic mesh face and intercepted by a generic camera pixel, hence introducing the view factor between the mesh face and the pixel:[10]

$$dQ_{fp} = \frac{\int_0^\infty \varepsilon(\lambda)\, B(\lambda, T)\, R(\lambda)\, d\lambda}{\pi} \frac{(\hat{\mathbf{n}}_f \cdot \mathbf{r}_{fp})\,(\hat{\mathbf{n}}_p \cdot \mathbf{r}_{pf})}{|\mathbf{r}_{fp}|^4}\, dA_f dA_p \tag{2}$$

Where $\hat{\mathbf{n}}_f$ is the mesh face normal versor, $\hat{\mathbf{r}}_{fp}$ is the position vector of the camera pixel relative to the mesh face center, $\hat{\mathbf{n}}_p$ is the normal versor of the pixel and $\mathbf{r}_{pf}$ is the mesh face center position relative to the camera pixel.

Given the small size of the pixels and their close positions, it is assumed that the view factors between one mesh face and all the camera pixels are equal, thus it is sufficient to compute the view factor between the mesh face and the full camera array, thus the formulation becomes:

DOI: 10.13009/EUCASS2023-751

$$dQ_{fc} = \frac{\int_0^\infty \varepsilon(\lambda)\, B(\lambda, T)\, R(\lambda)\, d\lambda}{\pi} \frac{(\hat{\mathbf{n}}_f \cdot \mathbf{r}_{fc})\,(\hat{\mathbf{n}}_c \cdot \mathbf{r}_{cf})}{|\mathbf{r}_{fc}|^4}\, dA_f dA_c \tag{3}$$

The formula needs to be integrated over the camera area and over the mesh face. This step is discretized assuming the mesh face is small enough to write the expression as:

$$\Delta Q_{fc} = \frac{\int_0^\infty \varepsilon(\lambda)\, B(\lambda, T)\, R(\lambda)\, d\lambda}{\pi} \frac{(\hat{\mathbf{n}}_f \cdot \mathbf{r}_{fc})\,(\hat{\mathbf{n}}_c \cdot \mathbf{r}_{cf})}{|\mathbf{r}_{fc}|^4}\, \Delta A_f \Delta A_c \tag{4}$$

In the step between Eqn. 3 and Eqn. 4 the part of the equation regarding the view factor is approximated using the following formula:

$$F_{fc} = \frac{1}{A_f} \int_{A_c} \int_{A_f} \frac{(\hat{\mathbf{n}}_f \cdot \mathbf{r}_{fc})\,(\hat{\mathbf{n}}_c \cdot \mathbf{r}_{cf})}{\pi\, |\mathbf{r}_{fc}|^4} dA_f dA_c \approx \frac{(\hat{\mathbf{n}}_f \cdot \mathbf{r}_{fc})\,(\hat{\mathbf{n}}_c \cdot \mathbf{r}_{cf})}{\pi\, |\mathbf{r}_{fc}|^4}\, \Delta A_c \tag{5}$$

As verified in,[16,17] such approximation is able to catch the correct values of the view factors. Dividing by the mesh face and considering a single diffuse value for the emissivity, the equation provides the heat flux per unit area emitted by each face:

$$q_{fc} = \frac{\Delta Q_{fc}}{\Delta A_f} = \frac{\varepsilon \int_0^\infty B(\lambda, T)\, R(\lambda)\, d\lambda}{\pi} \frac{(\hat{\mathbf{n}}_f \cdot \mathbf{r}_{fc})\,(\hat{\mathbf{n}}_c \cdot \mathbf{r}_{cf})}{|\mathbf{r}_{fc}|^4}\, \Delta A_c \tag{6}$$

Clearly to compute the heat flux the camera pose and attitude must be provided to the algorithm. The final result is a field of the heat flux emitted by each face intercepted by the camera. In this way, the image accounts for the view factors effects of the scene. The field is then passed to the render engine for the actual image generation. The method pipeline is summarized in Fig. 1

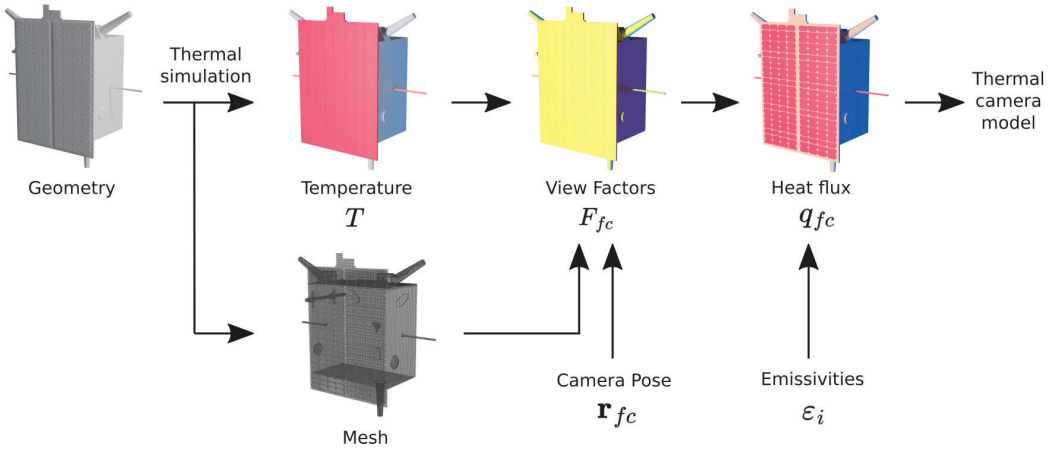

Figure 1: Method workflow

2.3 Thermal camera model

Microbolometer pixels produce an output voltage that is proportional to the heat flux received, such voltage is then amplified with a gain and converted to a digital bit string. The conversion is done by the analog-to-digital-unit ADU of the camera and the number of discretization intervals depends on the bit architecture of the ADU, for example for a 16 bit architecture there will be 2^{16} intervals also called digital numbers DN. The pixel output then is a DN whose value is proportional to the heat flux received.

The proposed approach for modelling the camera is to start from the image produced by the rendering software, by knowing the bit depth of the image (in Blender is either 8 or 16 bit) and the scale values it is possible to associate the pixel DN of the image with the corresponding heat flux value. Then using the sensor response curve it is possible to compute the actual DN produced by the camera, from there, the noises can be added and the output, in DN, is the actual image produced by the camera. Once the actual DN is obtained the sensor response function can be inverted again and the corresponding noisy heat flux is obtained and the radiative temperature recovered.

DOI: 10.13009/EUCASS2023-751

The sensor function can be modelled in various ways here are reported two sensor functions and the respective proposed implementation.

DN-temperature sensor function The first approach links DN to temperature with the following relation:[5]

$$DN = a \cdot T^{\alpha} + b \tag{7}$$

To compute a, b and α calibration is performed with a black body at different temperatures, the coefficient values are reported in.[5] In order to use such a model, the heat flux is recovered for each pixel using the image scale values, then it is converted into the corresponding radiative temperature assuming the body as a black body emitter and accounting for the object distance. The orientation of the faces is not considered but the effect of the distance is taken into account. If the distance is not compensated then the equivalent T_{rad} values would be extremely low. Then, the value is fed into the sensor function to compute the corresponding DN, such values are modified according to the noise models and the noisy temperature is recovered inverting the sensor function (Eqn.7). The scale of the image can be then adjusted accordingly to the selected temperature range. The steps are summarized in Eqn. 8

$$q_{fc} \rightarrow T_{rad} = \left(\frac{q_{fc}\, \pi\, |\mathbf{r}_{fc}|^2}{\sigma\, \Delta A_c} \right)^{1/4} \rightarrow DN = a \cdot T^{\alpha} + b \rightarrow DN_{noisy} = DN + Noise \rightarrow T_{rad+noise} = \left(\frac{DN_{noisy} - b}{a} \right)^{1/\alpha} \tag{8}$$

DN-heat flux sensor function The second approach follows the same steps as the previous one but using the following formula for the pixel output as[13]

$$DN = a \cdot F(T) + b \tag{9}$$

As for the previous case, the formula is calibrated using black bodies at different temperatures, for the exact coefficient values please refer to.[13] The steps are summarized in Eqn.

$$q_{fc} \rightarrow F(T) = \frac{q_{fc}\, \pi^2\, |\mathbf{r}_{fc}|^2}{\Delta A_c} \rightarrow DN = a \cdot F(T) + b \rightarrow DN_{noisy} = DN + Noise \rightarrow F_{noisy} = \frac{DN_{noisy} - b}{a} \tag{10}$$

With the above formulation, the radiative temperature can be recovered using the sensor calibration curve,[13] where each $F_{noisy}(T_{rad})$ value corresponds to a radiative temperature value.

In both approaches, in the inversion of Eqn. 6, the part relative to the faces-camera orientation is left out in order to retain such effects in the final output as presented in the results in the next section.

The temperature field can always be corrected with the real emissivity of the material thus recovering the kinetic temperature. Starting from the radiative temperature the kinetic one can be computed as:

$$T_{kin} = \frac{T_{rad}}{\varepsilon^{1/4}} \tag{11}$$

The team has implemented the above methods and is now testing the algorithms, where the image reporting the q_{fc} values is processed to extract the numerical values required as stated in the above formulations. The result will be presented in a future work with an emphasis on the camera modelling and noises.

3. Results

The section presents the results computed with the method presented in Section 2. As first point, it must be highlighted that once q_{fc} is computed it is possible to use it for the application of any thermal camera model. Indeed the results presented in the section focus on such quantity as everything in the final thermal image is proportional to it. Furthermore, since q_{fc} is scaled by the emissivity value of the material, it is clear that has a big impact on the final result as reported in the following subsections. The presented images are noiseless and for thermal images the black and white scale is set from zero to the max heat flux value of the scene, producing a realistic thermal image upon which given the thermal camera model presented in Section 2 the actual output of the instrument can be produced. The results are divided into two scenarios: spacecraft and asteroids.

DOI: 10.13009/EUCASS2023-751

3.1 Spacecraft

For the spacecraft scenario, the TANGO satellite is used as the future goal is to create a thermal image dataset equivalent to the ones already available in the optical spectrum.[4] Unfortunately, the exact TANGO spacecraft geometry is not accessible, nonetheless, a representative geometry made of multiple parts is created and each part is assigned with an emissivity value. The geometry is reported in Fig. 2 and it is made of 205 solar cells, 5 panels, 5 antennas, 7 patch antennas and one coil with 2 supports for a total of 225 parts. The emissivities of each part are reported in Tab. 1

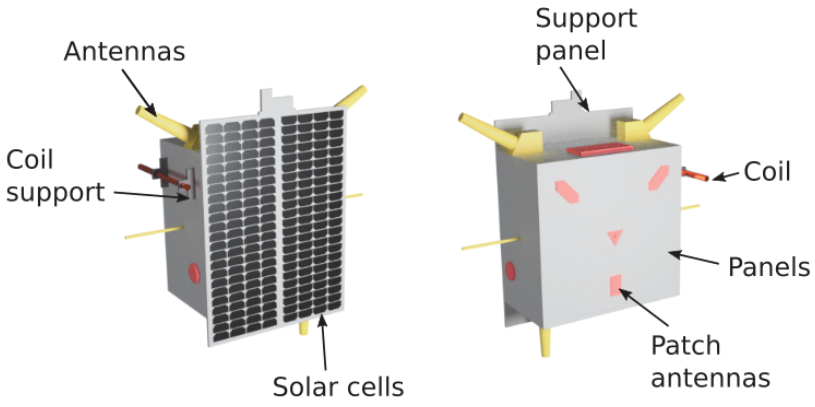

Figure 2: Tango geometry used for thermal simulation.

Table 1: Emissivity values

Part Name	Emissivity
Antennas	0.86
Patch antennas	0.90
Coil	0.86
Support coil	0.86
Panels	0.40
Solar cell	0.60

The first thing to highlight in the results is the effect of the different components emissivities. As clearly visible for a given camera pose reported in Fig. 3 the solar cells are isothermal with the support panel making them invisible in the temperature field image but due to the different emissivity the respective heat flux is much different with respect the support panel on which they are mounted on thus creating a sharp contrast in the image.

The same goes for the patch antenna, completely invisible as isothermal with the lateral panel, it stands out clearly in the thermal image. Furthermore, due to the different faces orientation of the patch antenna with respect to the camera, given its curved shape, it is possible to appreciate the effects of the view factors on the amount of heat flux intercepted by the camera. As the face normal is aligned closer to the camera normal the color is more bright and vice versa. The same consideration goes for other curved shapes such as the cylindrical antennas of TANGO (Fig. 3 top arrow). The effect of emissivities and view factors are even more visible for an arbitrary sequence of images taken from an orbit around the spacecraft pointing its center. As the solar panel normal gets closer to being perpendicular to the camera normal the heat flux intercepted lowers down as reported in the second and fourth row of Fig. 5. Please consider that to show the different orientations of the panels the frames are not taken at equal intervals, thus the second and fourth rows of frames have different angles with respect to the camera even though to the naked eye they look symmetric, this also highlights how small angle differences in the camera-object system can affect the results. The same considerations go for all the panels in general and in conclusion, the resulting black and white thermal image is reported in Fig. 4.

DOI: 10.13009/EUCASS2023-751

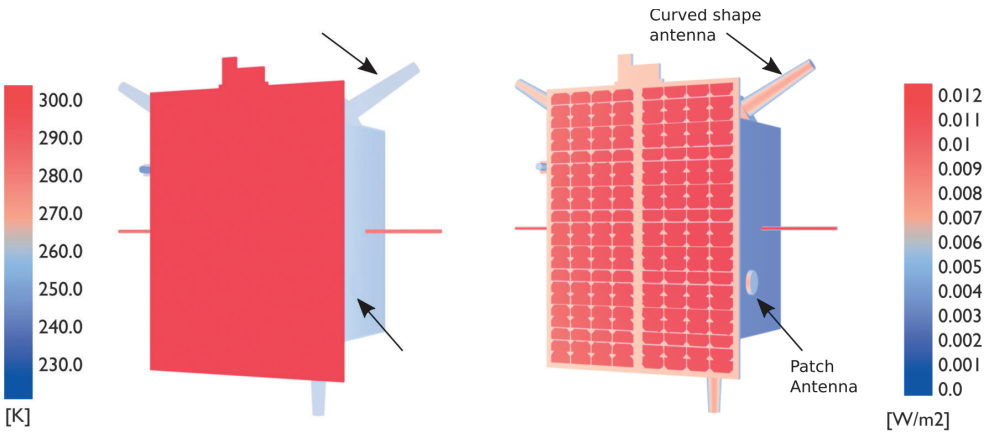

Figure 3: Tango temperature field (left) and radiance field intercepted by the camera q_{fc} (right).

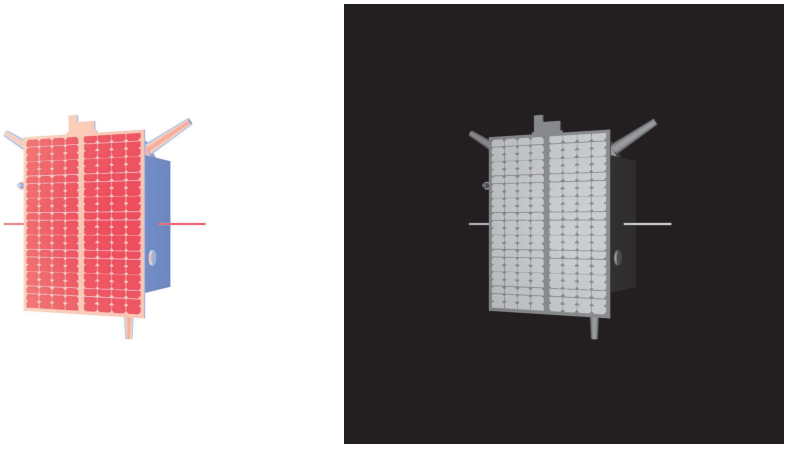

Figure 4: radiance field q_{fc}(left) infrared image black and white image (right)

DOI: 10.13009/EUCASS2023-751

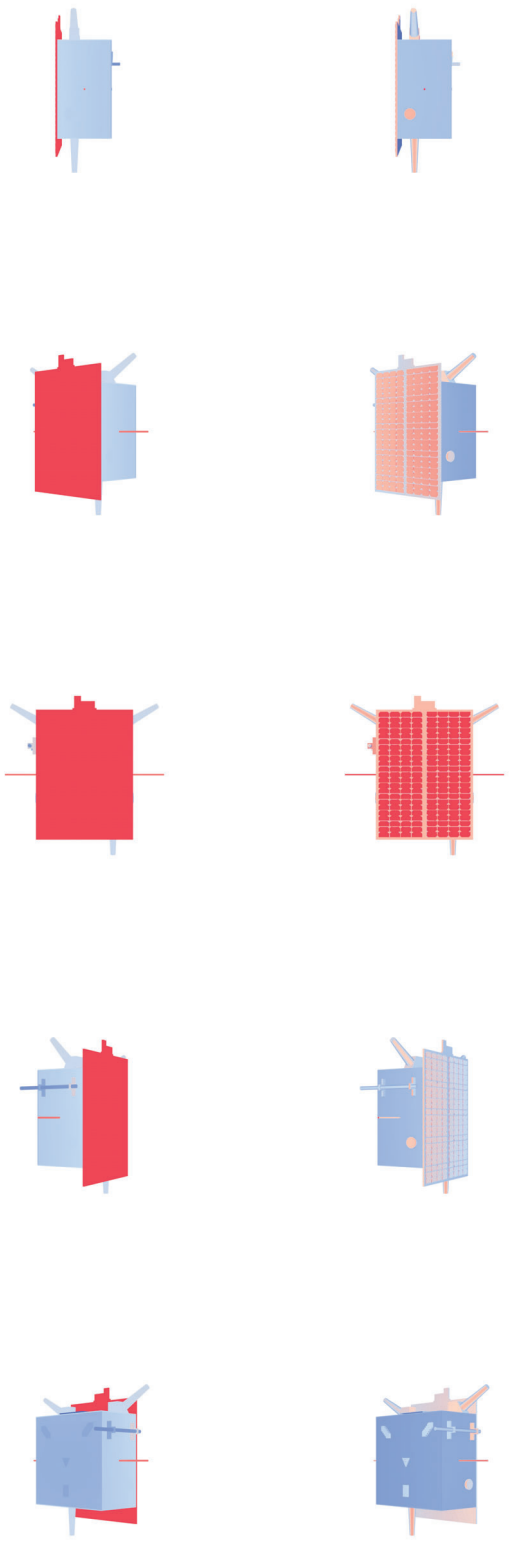

Figure 5: Temperature field (left) radiance field q_{fc} (right)

DOI: 10.13009/EUCASS2023-751

3.2 Asterorid

For the asteroid case, Ryugu has been selected as thermal images from the Hayabusa mission are available thus enabling future validation of the results. Furthermore, Ryugu geometry is freely available, on the other hand, all the files have corrupted geometry that must be cleaned before the thermal simulation. Some example of corrupted geometry is reported in Fig. 6, such regions are cleaned using smoothing filters and sculpting techniques available in Blender.

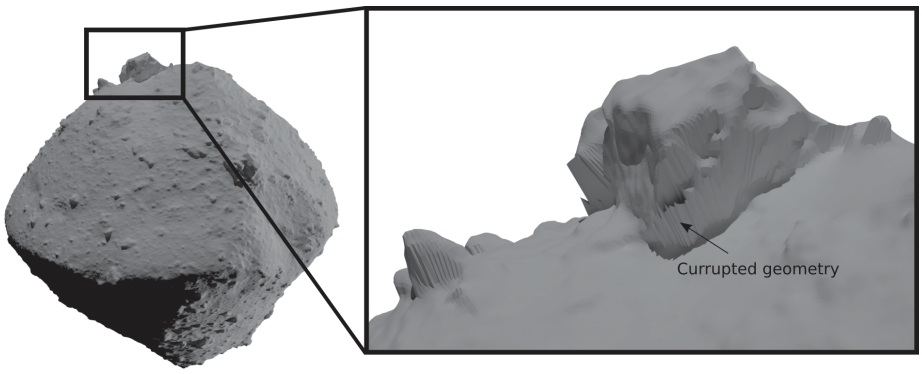

Figure 6: Ryugu 3M model corrupted geometry region.

The model used for the simulation is the 3M one which thanks to the higher resolution helps the meshing algorithm to catch all the terrain shapes.

The number of cells on the Ryugu exterior face is increased in the snapping parameters to overcome radiation illness of the linear system produced in the finite volume discretization process. Due to the low conductivity of the asteroid regolith, at the surface of Ryugu, where radiation and diffusion are combined, radiation overcomes diffusion for each cell at that surface. This creates instability due to the big oscillations caused by the errors in the temperature field that are elevated to the power of 4 in the code. To better clarify the problem the code has been benchmarked with a cube of 12 m and with different mesh discretizations. The analysis of such a problem is out of the scope of the article but in conclusion, reducing the cell size and using relaxation is enough to stabilize the algorithm. Given the problem though, different mesh resolutions were tested to verify the results were correct at least from a numerical point of view.

The final simulation is single material and it is run in steady state mode, moreover, to avoid losing convergence in the first steps, the simulation is started with a high conductivity value at $270\,\mathrm{W\,m^{-1}\,K^{-1}}$ and once convergence is reached it is lowered to $1\,\mathrm{W\,m^{-1}\,K^{-1}}$, thus ensuring a starting temperature field closer to the final one hence reducing the initial temperature oscillations given by the guessed starting temperature field. All the mesh sizes tested to prove the numerical convergence of the grid are reported in Tab. 2.

Table 2: Ryugu simulation stabilizes at 6M faces on asteroid surface.

Ryugu Face N Cells	Ryugu Face Cell [m]	Min [K]	Max [K]	Note
3.7M	0.4	-340	1280	Oscillation
4.3M	0.36	77	800	Oscillation
5.7M	0.33	40	418	Stable
6.4M	0.31	40	416	Stable
8.9M	0.26	42	419	Stable

The final temperature field is reported in Fig. 7, the level of detail that can be reached from the tool is very high but of course in this case the computational cost is much higher with respect to the other case.

As for the spacecraft case, the view factors play a big role. In Fig. 8 it is clear how the curved shape of the object lowers the view factors moving from the equator region towards the polar region, as a consequence the heat flux intercepted by the camera is higher when looking at the equator. To better clarify this point, a sequence of frames is taken using a circular orbit around the asteroid with the camera facing the center, from Fig. 9 it is possible to see how the rocks and faces parallel to the camera create bright contrasts producing a realistic thermal image. As an example of the final output in black and white scale, a frame is reported in Fig. 10.

DOI: 10.13009/EUCASS2023-751

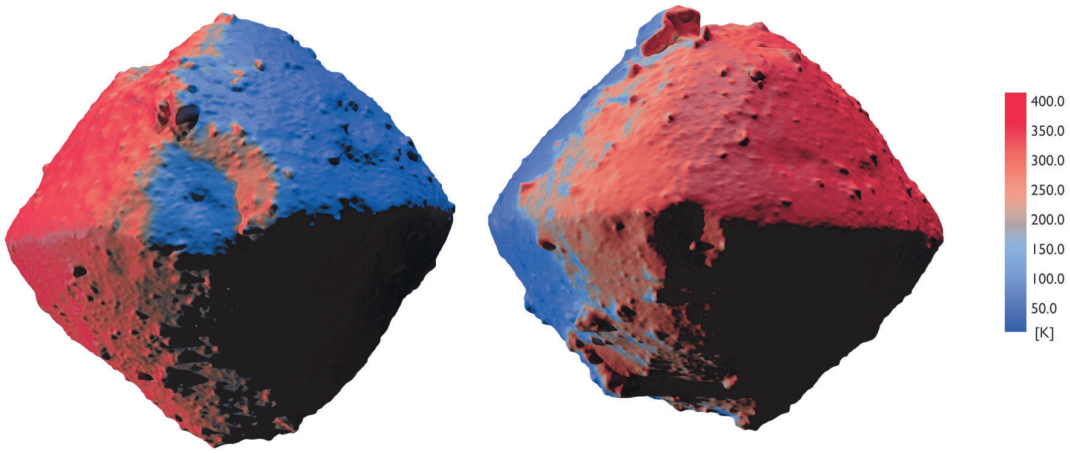

Figure 7: Ryugu temperature field rendering (light and shadows just to better visualize terrain, not coherent with temperature field).

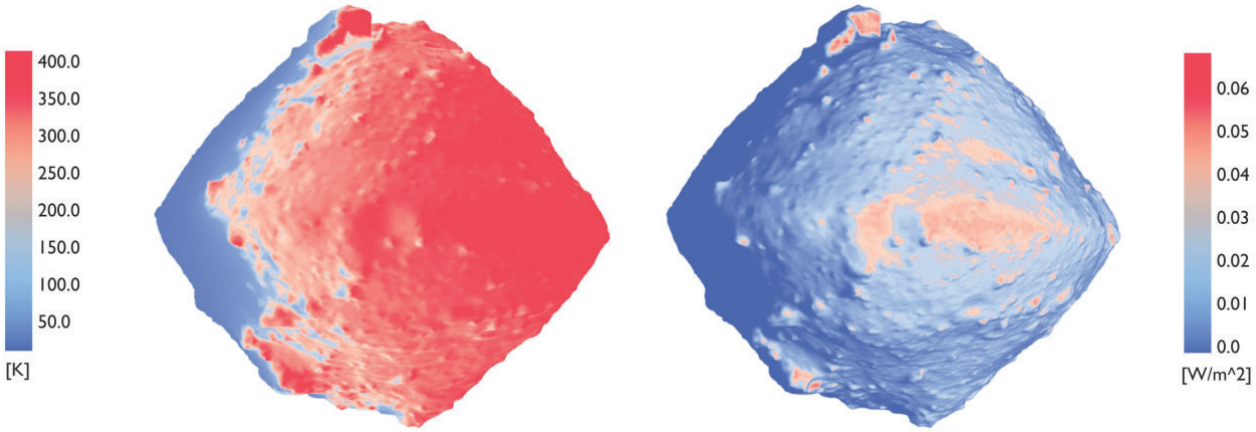

Figure 8: Ryugu temperature field (left) and radiance field $q_f c$ (right)

DOI: 10.13009/EUCASS2023-751

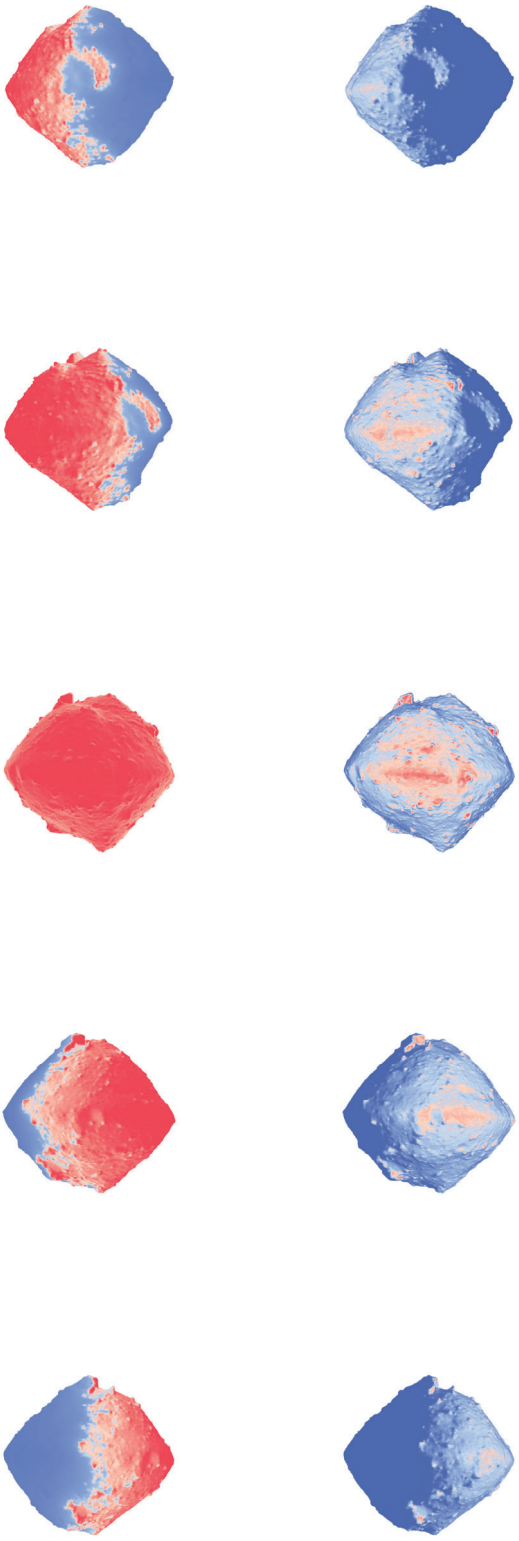

Figure 9: Temperature field (left) radiance field q_{fc} (right)

DOI: 10.13009/EUCASS2023-751

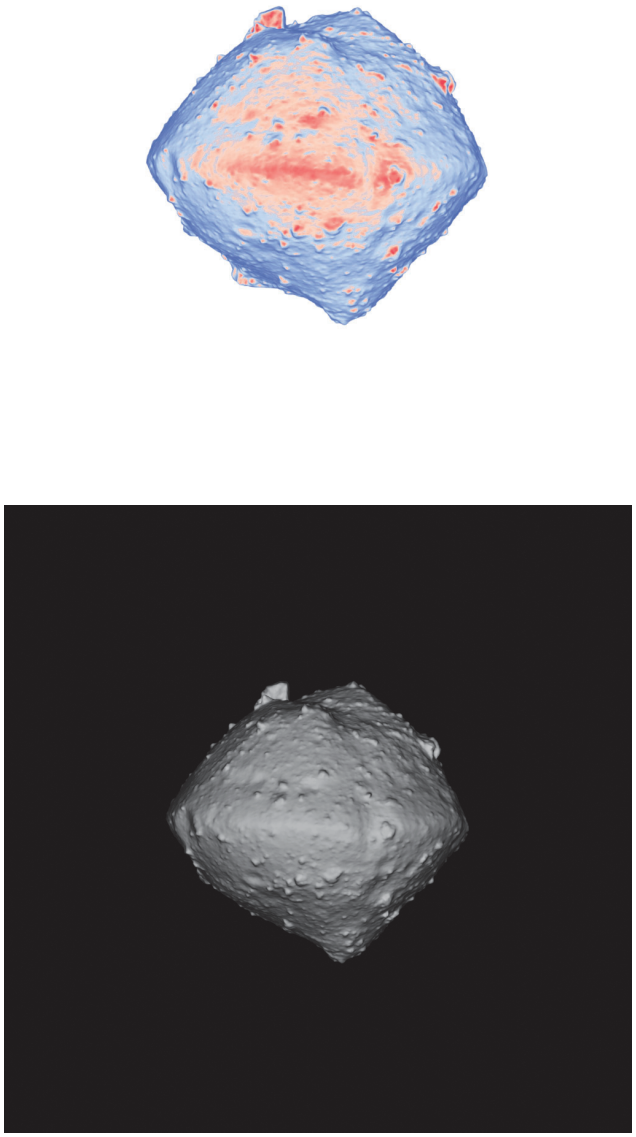

Figure 10: Radiance field q_{fc}(top) infrared image black and white image (bottom)

DOI: 10.13009/EUCASS2023-751

4. Applications and Conclusions

4.1 Applications

The tool has many applications, the preliminary results of the tool were applied in[3,6–8] for image fusion with the goal to enhance optical image visibility using thermal infrared camera data.

The tool is used also for far-range detection where the advantages of the thermal image are clearer. The object analysed in this case is the VESPA debris at a 100 m distance (the reader can refer to[4,8] for more information), the thermal image is compared with the respective visual one in Fig. 11. As stated in the introduction the visible image capture all the star lights making it harder to detect compared to the thermal infrared image where it is a bright light point. The same goes for long-exposure images in Fig. 12, (credits to M.Bechini for the images in the visible spectrum[4]).

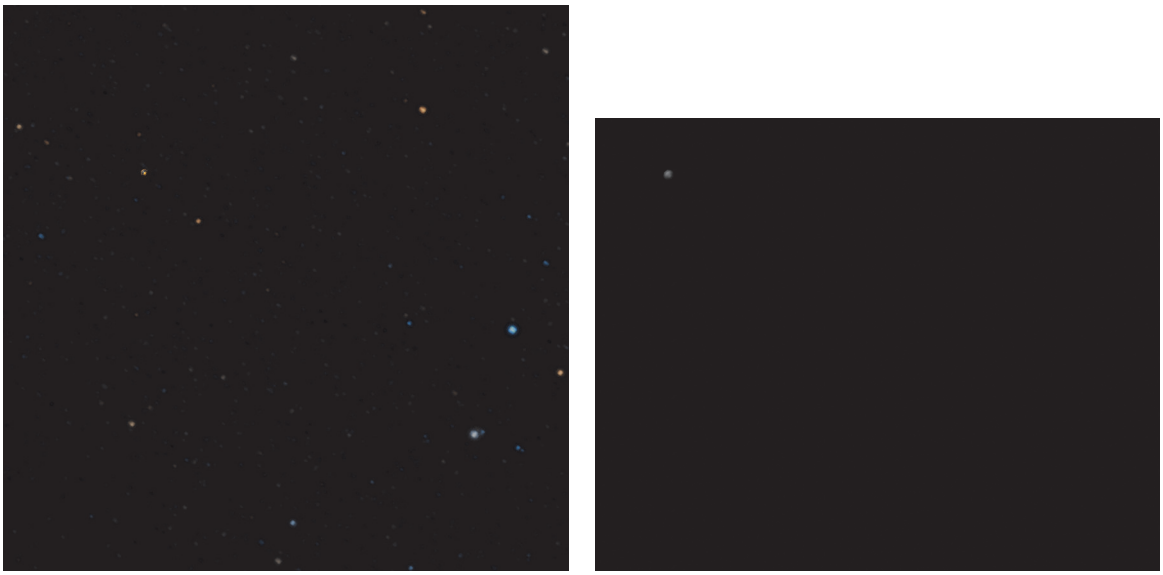

Figure 11: Visible image with stars (left) and thermal image (right)

Figure 12: Inertial pointing visible image with stars (left) and thermal image (right)

Of course, in a real scenario as reported in[12] the camera noise level and response function must be modelled as presented in Section 2 to clearly asses the detection range of the object.

DOI: 10.13009/EUCASS2023-751

4.2 Conclusions

The presented tool proposes a methodology to create synthetic thermal infrared images enabling the simulation of the infrared camera output given the camera position and attitude. It is demonstrated how the tool creates realistic thermal images in both spacecraft and asteroid proximity scenarios and both in single and multi-material cases, proving to be suited for multiple mission cases. Furthermore, two camera models are presented and they can be used as starting points for the production of realistic instrument output. The presented work is a step in the existing literature as no methodologies to produce synthetic infrared images from thermal simulations have ever been presented up to the authors' knowledge. The approach can be repeated and implemented by any other research team since all the software used are open source and free of license thus making the method available to anyone interested in the research. The future works are focused on introducing thermal images of Earth as background for LEO operations and the second focus is on the camera modelling, for both points codes are already been created and they are now being tested and will be presented in the next research outcome.

DOI: 10.13009/EUCASS2023-751

References

[1] The Ultimate Infrared Handbook for R&D Professionals, May 2023. [Online; accessed 28. May 2023].

[2] Takehiko Arai, Tomoki Nakamura, Satoshi Tanaka, Hirohide Demura, Yoshiko Ogawa, Naoya Sakatani, Yamato Horikawa, Hiroki Senshu, Tetsuya Fukuhara, and Tatsuaki Okada. Thermal Imaging Performance of TIR Onboard the Hayabusa2 Spacecraft. *Space Science Reviews*, 208(1):239–254, July 2017.

[3] Michele Bechini, Gaia Letizia Civardi, Matteo Quirino, Alessandro Colombo, and Michelle Lavagna. Robust Monocular Pose Initialization via Visual and Thermal Image Fusion. *ResearchGate*, September 2022.

[4] Michele Bechini, Michèle Lavagna, and Paolo Lunghi. Dataset generation and validation for spacecraft pose estimation via monocular images processing. *Acta Astronautica*, 204, March 2023.

[5] E. Brageot, O. Groussin, P. Lamy, and J.-L. Reynaud. Experimental study of an uncooled microbolometer array for thermal mapping and spectroscopy of asteroids. *Experimental Astronomy*, 38(3):381–400, December 2014.

[6] Gaia Letizia Civardi, Michele Bechini, Alessandro Colombo, Matteo Quirino, Margherita Piccinin, and Michelle Lavagna. VIS-TIR Imaging for Uncooperative Objects Proximity Navigation: a Tool for Development and Testing. *ResearchGate*, June 2022.

[7] Gaia Letizia Civardi, Michele Bechini, Matteo Quirino, Alessandro Colombo, Margherita Piccinin, and Michèle Lavagna. Generation of fused visible and thermal-infrared images for uncooperative spacecraft proximity navigation. *Advances in Space Research*, March 2023.

[8] Alessandro Colombo, Gaia Letizia Civardi, Michele Bechini, Matteo Quirino, and Michelle Lavagna. VIS-TIR cameras data fusion to enhance relative navigation during In Orbit Servicing operations. *ResearchGate*, September 2022.

[9] Marco Delbo, Michael Mueller, Joshua P. Emery, Ben Rozitis, and Maria Teresa Capria. Asteroid thermophysical modeling. *ArXiv e-prints*, August 2015.

[10] J. H. Lienhard, IV and J. H. Lienhard, V. *A Heat Transfer Textbook*. Phlogiston Press, Cambridge, MA, 5th edition, August 2020. Version 5.10.

[11] Tatsuaki Okada. Thermography of Asteroid and Future Applications in Space Missions. *Applied Sciences*, 10(6):2158, March 2020.

[12] Tatsuaki Okada, Tetsuya Fukuhara, Satoshi Tanaka, Makoto Taguchi, Takehiko Arai, Hiroki Senshu, Hirohide Demura, Yoshiko Ogawa, Toru Kouyama, Naoya Sakatani, Jun Takita, Tomohiko Sekiguchi, Jorn Helbert, Thomas G. Mueller, and Axel Hagermann. Earth and moon observations by thermal infrared imager on Hayabusa2 and the application to detectability of asteroid 162173 Ryugu. *Planetary and Space Science*, 158:46–52, September 2018.

[13] Tatsuaki Okada, Tetsuya Fukuhara, Satoshi Tanaka, Makoto Taguchi, Takeshi Imamura, Takehiko Arai, Hiroki Senshu, Yoshiko Ogawa, Hirohide Demura, Kohei Kitazato, Ryosuke Nakamura, Toru Kouyama, Tomohiko Sekiguchi, Sunao Hasegawa, Tsuneo Matsunaga, Takehiko Wada, Jun Takita, Naoya Sakatani, Yamato Horikawa, Ken Endo, Jörn Helbert, Thomas G. Müller, and Axel Hagermann. Thermal Infrared Imaging Experiments of C-Type Asteroid 162173 Ryugu on Hayabusa2. *Space Science Reviews*, 208(1):255–286, July 2017.

[14] I. Pelivan. Thermophysical modelling for high-resolution digital terrain models. *Monthly Notices of the Royal Astronomical Society*, 478(1):386–398, July 2018.

[15] Margherita Piccinin, Gaia Letizia Civardi, Matteo Quirino, and Michèle Lavagna. Multispectral Imaging Sensors for asteroids relative navigation. *ResearchGate*, October 2021.

[16] Matteo Quirino, Luca Marocco, Manfredo Guilizzoni, and Michèle Lavagna. High Energy Rapid Modular Ensemble of Satellites Payload Thermal Analysis Using OpenFOAM. *Journal of Thermophysics and Heat Transfer*, March 2021.

[17] Matteo Quirino, Giulia Sciarrone, Raffaele Piazzolla, Fabio Fuschino, Yuri Evangelista, Gianluca Morgante, Manfredo Guilizzoni, Luca Marocco, Stefano Silvestrini, Fabrizio Fiore, and Michèle Lavagna. HERMES CubeSat Payload Thermal Balance Test and Comparison with Finite Volume Thermal Model. *Applied Sciences*, 13(9):5452, April 2023.